Proceedings of the
Annual Stability Conference
Structural Stability Research Council
St. Louis, Missouri, April 2-5, 2019

Validation study of a new inelastic material model for steel W-Shapes

Barry T. Rosson[1], Ronald D. Ziemian[2]

Abstract
The stiffness reduction of compact W-Shapes with an ECCS residual stress pattern was studied in detail using a fiber element model with over 2,000 elements. For a given moment, axial load and residual stress ratio, the distribution of stresses throughout the cross-section and associated reduced stiffness were evaluated and used to develop an inelastic material model for use as normalized tangent modulus expressions in *MASTAN2*. The material model's ability to develop realistic column strength curves over a range of W-Shape dimensions was studied. Ultimate load analyses were conducted on five benchmark frames using the new material model and were compared with the results obtained using advanced nonlinear finite element models. Discussion and recommendations are provided regarding the material model and its ability to determine the ultimate load capacity of different types of frames and loading conditions.

1. Introduction

Appendix 1 of the *Specification for Structural Steel Buildings* (2017) provides the designer with the option to use advanced methods of structural analysis to directly model localized yielding and its effects on system behavior. The analysis requirements stipulate that: a second-order inelastic analysis is necessary; the material properties and yield criteria are to be reduced by a factor of 0.9; the geometric imperfections shall be directly modeled such that it develops the greatest destabilizing effect; and the influence of residual stress and partial yielding effects are to be considered. Recent research has focused on developing improved empirical relationships to account for the reduction in stiffness that occurs due to yielding of the beam-column's cross-section (Zubydan 2011; Kucukler *et al*. 2014, 2016; Rosson 2017, 2018). The purpose of this study is to investigate the effectiveness of a new inelastic material model to correctly account for the loss of stiffness in W-Shape columns with uniaxial bending and to accurately predict the ultimate load capacity of steel frames.

2. Stiffness Reduction m-p-τ Surface Plot Perimeter Conditions

The stiffness reduction (τ) that results from yielding of the cross-section due to major- or minor-axis bending and axial load was studied in detail using a fiber element model for W-Shapes with an ECCS (1984) residual stress pattern (Rosson 2017). The model used 2,046 fiber elements over

[1] Professor, Florida Atlantic University, <rosson@fau.edu>
[2] Professor, Bucknell University, <ziemian@bucknell.edu>

the cross-section (400 fiber elements in each flange and 1,246 fiber elements in the web). For a given normalized moment m (M/M_p), axial load p (P/P_y), and residual stress ratio c_r (σ_r/σ_y), the stiffness reduction was carefully assessed for a W8x31 with c_r = 0.3. Throughout the paper p is understood to be positive such that the sign on P_y matches that of the applied axial load P. Bending about the minor-axis is understood to have a normalized moment $m = M/M_{py}$, and bending about the major-axis is understood to have a normalized moment $m = M/M_{px}$.

Using the m and p results with increments of 0.01, over 7,000 data points were used to produce the m-p-τ surface plot in Fig. 1 for minor-axis bending and axial compression, and in Fig. 2 for major-axis bending and axial compression.

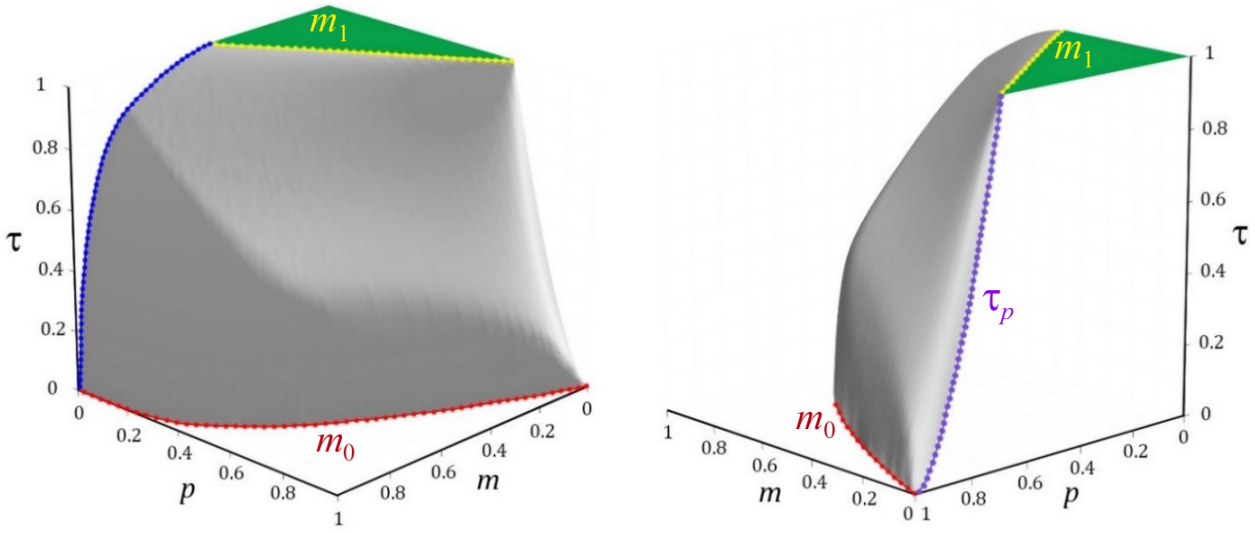

Figure 1: W8x31 minor-axis bending and axial compression m-p-τ surface plot perimeter conditions for c_r = 0.30

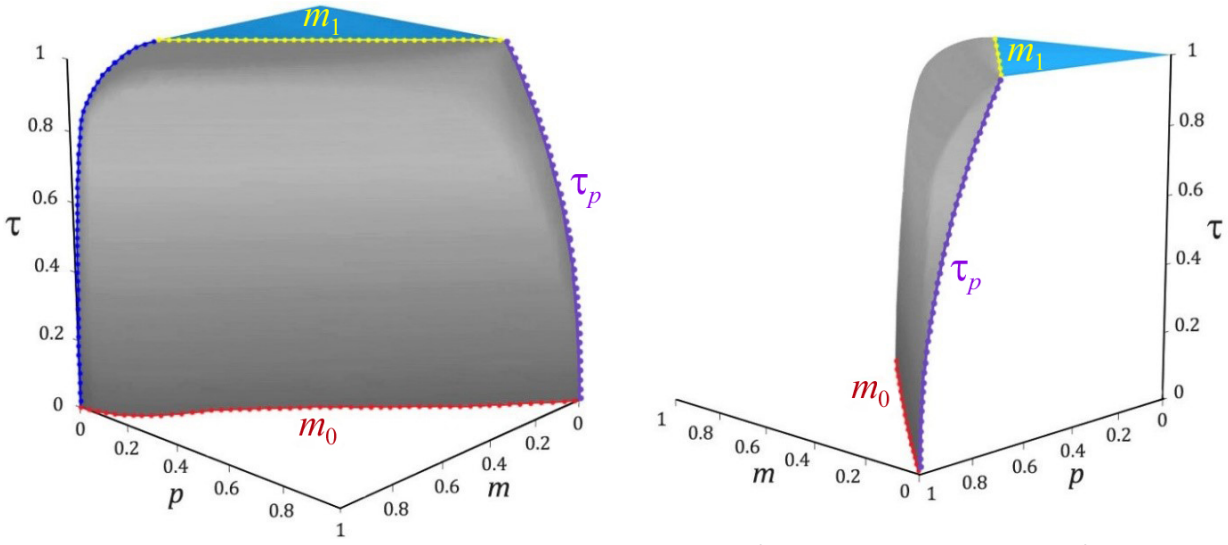

Figure 2: W8x31 major-axis bending and axial compression m-p-τ surface plot perimeter conditions for c_r = 0.30

2.1 m and p conditions at the limit of $\tau = 1$ (yellow line in Figs. 1 and 2)

The equation to determine the extent of $\tau = 1$ is found in the literature (Attalla *et al*. 1994; Zubydan 2011; Rosson 2016). For a given residual stress ratio c_r and axial compression load condition p, the maximum moment at which $\tau = 1$ is maintained is given as

$$m_1 = \frac{S_y}{Z_y}(1 - c_r - p) \tag{1}$$

where S_y is the minor-axis elastic section modulus and Z_y is the minor-axis plastic section modulus. The maximum moment at which $\tau = 1$ is maintained for the major-axis bending and axial compression condition is determined in a similar manner and is found to be

$$m_1 = \frac{S_x}{Z_x}(1 - c_r - p) \tag{2}$$

where S_x is the major-axis elastic section modulus and Z_x is the major-axis plastic section modulus.

2.2 m = 0 and p > 1 – c_r (purple line in Figs. 1 and 2)

To determine the stiffness reduction τ for a given p and c_r condition, the minor-axis moment of inertia of the remaining cross-section that has not yielded is divided by the original minor-axis moment of inertia I_y. The relationship for τ is found to be

$$\tau_p = \frac{2\left(\sqrt{\frac{1-p}{c_r}}\right)^3 + \lambda\lambda_o^2\sqrt{\frac{1-p}{c_r}}}{2 + \lambda\lambda_o^2} \tag{3}$$

where $\lambda = A_w / A_f$ and $\lambda_o = t_w / b_f$ (Rosson 2016). For W-Shapes in which $\lambda\lambda_o{}^2$ is very small compared to 2, a very close approximation to Eq. 3 excludes the effect of the web and is given as

$$\tau_p = \left(\sqrt{\frac{1-p}{c_r}}\right)^3 \tag{4}$$

The stiffness reduction τ for the major-axis condition is determined in a similar manner and is found to be

$$\tau_p = \frac{\lambda\lambda_1^2\left[1 - \left(1 - \sqrt{\frac{1-p}{c_r}}\right)^3\right] + \sqrt{\frac{1-p}{c_r}}[2 + 6(1+\lambda_1)^2]}{\lambda\lambda_1^2 + 2 + 6(1+\lambda_1)^2} \tag{5}$$

where $\lambda_1 = d_w / t_f$ (Rosson 2017). Eqs. 3 through 5 are based on the assumed shape of the residual pattern; therefore, the shape of the purple lines in Figs. 1 and 2 are unique to the ECCS residual stress pattern.

2.3 m and p conditions for $\tau = 0$ (red line in Figs. 1 and 2)

Two equations are needed to determine the m and p conditions when $\tau = 0$ for both minor- and major-axis bending. For the minor-axis bending with axial compression condition, one equation is needed when the plastic neutral axis is inside the web thickness, and the other equation is needed when it is outside the web thickness. Closed-form equations are given in the book by Chen and Sohal (1995); however, the same results can be obtained with fewer computations using the constants λ, λ_o and λ_1 (Rosson 2016).

$$m_0 = 1 - \frac{p^2(2+\lambda)^2}{(2+\lambda\lambda_o)(2+\lambda_1)} \tag{6}$$

$$when\ p \geq \frac{2\lambda_o + \lambda}{2+\lambda} \qquad m_0 = \frac{4 - [p(2+\lambda) - \lambda]^2}{2(2+\lambda\lambda_o)} \tag{7}$$

For the major-axis bending with axial compression condition, one equation is needed when the plastic neutral axis is outside the flange thickness, and the other equation is needed when it is inside the flange thickness.

$$m_0 = 1 - \frac{p^2(2+\lambda)^2}{4\lambda_o + \lambda(4+\lambda)} \tag{8}$$

$$when\ p \geq \frac{\lambda}{2+\lambda} \qquad m_0 = \frac{(2+\lambda_1)^2 - [p(2+\lambda) - \lambda + \lambda_1]^2}{4 + \lambda_1(4+\lambda)} \tag{9}$$

Eqs. 6 through 9 do not depend upon the assumed shape of the residual pattern; therefore, the shape of the red lines in Figs. 1 and 2 are unaffected by the ECCS residual stress pattern.

3. Material Models Based on *m-p-τ* Surface Plots

The equations presented for the yellow, purple and red lines in Figs. 1 and 2 are used as a basis to develop an inelastic material model for W-Shape sections. The extent of the triangular-shaped plateau region at which $\tau = 1$ for a given p and c_r condition is defined by m_1 from Eqs. 1 and 2. The stiffness when $m = 0$ for a given $p > 1 - c_r$ condition is defined by τ_p from Eqs. 3 and 5, and the conditions at which $\tau = 0$ for a given p condition are defined by m_0 from Eqs. 6 through 9. The shape of the gray shaded regions in Figs. 1 and 2 are dependent upon the cross-section dimensions and the maximum stress σ_r of the ECCS residual stress pattern. Similar equations to determine τ in the gray shaded regions cannot be written in closed-form and thus require an iterative solution technique. The following inelastic material models are given in closed-form are bound by m_1, τ_p and m_0, but they approximate the gray shaded regions in Figs. 1 and 2.

3.1 New inelastic material model

The new inelastic material model takes advantage of the closed-form equations for the perimeter conditions given by m_1, τ_p and m_0. The 3D surfaces in Figs. 1 and 2 for both the minor-axis bending and major-axis bending conditions are closely approximated using Eqs. 10 and 11. An appropriate value for the exponent n is selected based on fiber element *m-p-τ* results for a given W-Shape and the axis about which bending occurs.

$$\tau = 1 - \left(\frac{m - m_1}{m_0 - m_1}\right)^n \tag{10}$$

$$when\ p \geq 1 - c_r \qquad \tau = \tau_p \left[1 - \left(\frac{m}{m_0}\right)^n\right] \tag{11}$$

For a given axial compression p condition, and a W-Shape with its λ, λ_o, λ_1 and c_r constants, the m_1, τ_p and m_0 values are evaluated from Eqs. 1, 3, 6 and 7 for minor-axis bending, and Eqs. 2, 5, 8 and 9 for major-axis bending. In the absence of any other effort to determine an appropriate n value for a given W-Shape, it is recommended that n = 2 be used for minor-axis bending and n = 4 for major-axis bending. As illustrated in Fig. 3, for a given p and its corresponding m_1, τ_p and m_0 values, τ is evaluated based on the magnitude of the bending moment m. If $p < 1 - c_r$ and $m \leq m_1$, there is no stiffness reduction and $\tau = 1$. If $p < 1 - c_r$ and $m > m_1$, there is stiffness reduction between 1 and 0 along the light yellow line depending on the magnitude of m (using Eq. 10). If $p \geq 1 - c_r$, then stiffness reduction is between τ_p and 0 along the light blue line depending on the magnitude of m (using Eq. 11). If $m \geq m_0$ for any given p condition, then $\tau = 0$.

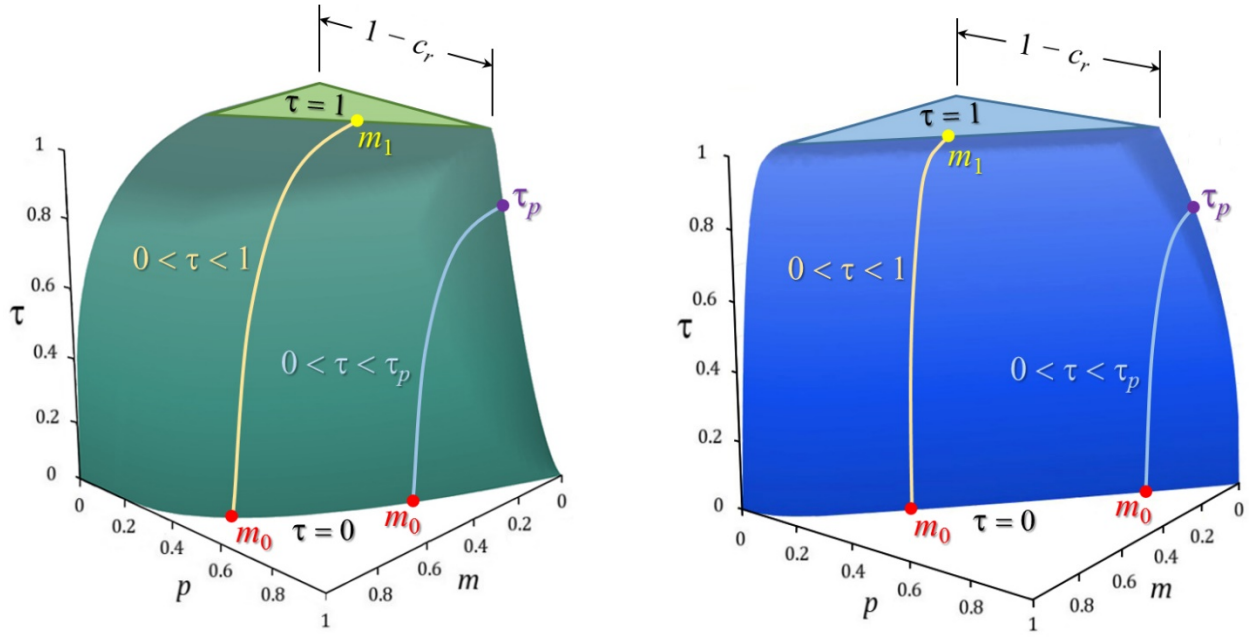

(a) (b)

Figure 3: m-p-τ surface plots from Eqs. 10 and 11 for a) minor-axis bending and b) major-axis bending

3.2 Fiber element polynomial

The fiber element data used to create Fig. 1 were used to generate a nonlinear regression model for τ in terms of both m and p for the minor-axis bending condition and c_r = 0.3 (Rosson 2016). Only the data in the gray shaded region of Fig. 1 were used to determine the nonlinear regression coefficients. Based on the results from several trial models, the polynomial provided in Eq. 12 was

found to provide the best r^2 values. With the coefficients as given in Table 1, $r^2 = 0.99$ ($n = 4{,}832$) for $0 \le p < 0.7$ and $r^2 = 0.98$ ($n = 1{,}042$) for $0.7 \le p \le 1.0$.

$$\tau = a_0 + a_1 m + a_2 m^2 + a_3 m^4 + a_4 m^6 + a_5 m^8 + a_6 p + a_7 p^2 + a_8 p^4 + a_9 p^6 + a_{10} p^8 + a_{11} mp + a_{12} m^2 p^2 + a_{13} m^4 p^4 \quad (12)$$

Table 1: Nonlinear regression model coefficients for W8x31 with minor-axis bending

Coefficients	$0 \le p < 0.7$	$0.7 \le p \le 1.0$
a_0	1.233	-4.976
a_1	-0.9771	-8.224
a_2	1.739	3.425
a_3	-4.870	29.76
a_4	8.364	-76.82
a_5	-5.338	66.64
a_6	1.400	28.48
a_7	-3.863	-38.51
a_8	7.654	29.67
a_9	-12.89	-23.91
a_{10}	7.000	9.239
a_{11}	-2.377	10.26
a_{12}	4.757	-11.78
a_{13}	-13.31	-22.64

3.3 Stiffness matrix used for modeling the distributed plasticity

Since the bending moments usually vary along the length of the beam-column, the stiffness reduction over the member length must also be accounted for when yielding occurs. An easy and effective way of accomplishing this is to assume the tangent modulus varies linearly over the length of the element. In practice, the error introduced by this assumption is reduced by using multiple elements along the length of the member, and especially in locations of high moment gradient. The closed-form stiffness matrix developed by Ziemian and McGuire (2002) was used for this study because the τ values from Eqs. 10 through 12 can be used directly as the a and b terms in Eq. 13. The a term is the τ condition based on the m and p conditions at the start of the element, and the b term is based on the m and p conditions at the end of the element.

$$[k] = \frac{EI}{L}\begin{bmatrix} \frac{12}{L^2}\left(\frac{a+b}{2}\right) & -\frac{6}{L}\left(\frac{2a+b}{3}\right) & -\frac{12}{L^2}\left(\frac{a+b}{2}\right) & -\frac{6}{L}\left(\frac{a+2b}{3}\right) \\ & 4\left(\frac{3a+b}{4}\right) & \frac{6}{L}\left(\frac{2a+b}{3}\right) & 2\left(\frac{a+b}{2}\right) \\ & & \frac{12}{L^2}\left(\frac{a+b}{2}\right) & \frac{6}{L}\left(\frac{a+2b}{3}\right) \\ & Sym. & & 4\left(\frac{a+3b}{4}\right) \end{bmatrix} \quad (13)$$

The stiffness matrix in Eq. 13 is already a part of the nonlinear material capabilities of *MASTAN2* (2015). The computer program also contains incremental analysis routines for modeling the

nonlinear geometric behavior. Eqs. 10 through 12 were implemented in a nonlinear material subroutine of *MASTAN2*. For a given W-Shape section, the constants λ, λ_o, λ_1 and c_r were input, and for a given p condition Eqs. 1 and 2 were used to evaluate m_1 (limit on the extent of $\tau = 1$), Eqs. 3 and 5 were used to evaluate τ_p, and Eqs. 6 through 9 were used to evaluate m_0 (boundary of $\tau = 0$). With m_1, τ_p and m_0 defined for a given p condition of an element, the m condition at each end of the element was used in Eqs. 10 through 12 to generate the a and b terms in Eq. 13.

4. Column Strength Study

Column limit load analyses were conducted on pinned-pinned columns using the new material model (Eqs. 10 and 11) and were compared with various other column strength analysis results. All of the member cross-sections were assumed to be fully-compact and their out-of-plane behavior fully restrained. All column analyses were conducted using a second-order inelastic analysis with the full modulus of elasticity and yield stress. The initial geometric imperfections were directly modeled using the first eigen-mode normalized to $L/1000$ at mid-height. The columns were modeled with *MASTAN2*, and in all cases 10 line elements were used with $n = 2$ for minor-axis bending and $n = 4$ for major-axis bending.

The limit load analysis results of a W8x31 with minor-axis bending are given in Fig. 4. The new material model results are compared with Eqs. (E3-2) and (E3-3) of the *Specification for Structural Steel Buildings* (2017) and the results from a similar *MASTAN2* model with 10 line elements but with τ defined by the fiber element polynomial as given in Eq. 12 and the coefficients in Table 1. A comparison of the curves indicates that the fiber element polynomial more closely follows the *Specification* curve, and that due to the error introduced by approximating the gray surface in Fig. 1 with the 3D surface in Fig. 3a, the new model with $n = 2$ gives slightly lower results for $L/r < 50$ and slightly higher results for $50 < L/r < 100$. All three curves are very similar for $L/r > 100$ where the response is primarily elastic along the length of the column.

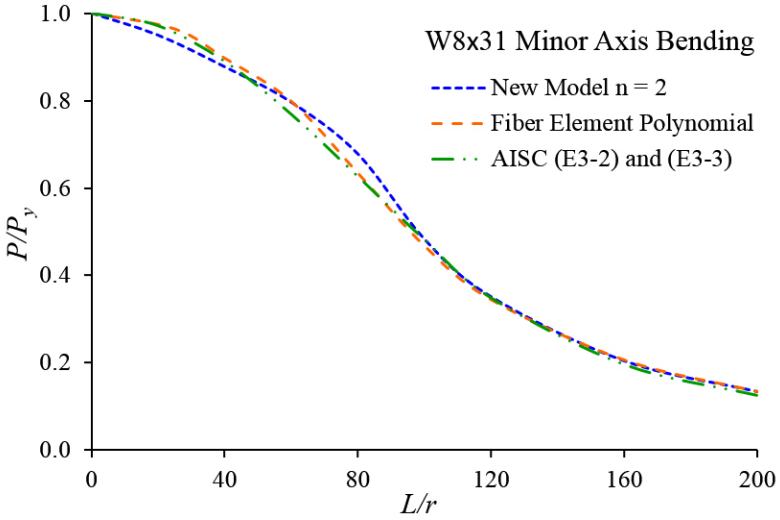

Figure 4: Column strength comparison of W8x31 with minor-axis bending

The effect of the assumed maximum residual stress on the column strength is illustrated in Fig. 5. As discussed in Shayan *et al*. (2014) and Rosson (2018), the range of c_r values between 0.18 and

0.42 is based on scale factors that vary by a maximum of two standard deviations of the mean residual stress of $0.3\sigma_y$. It is noticed in Fig. 5 that the magnitude of maximum residual stress affects the column strength results only in the range of approximately $50 < L/r < 100$. The results are given only for the W10x45 column with major-axis bending, but these results are consistent with those given by Shayan *et al*. (2014).

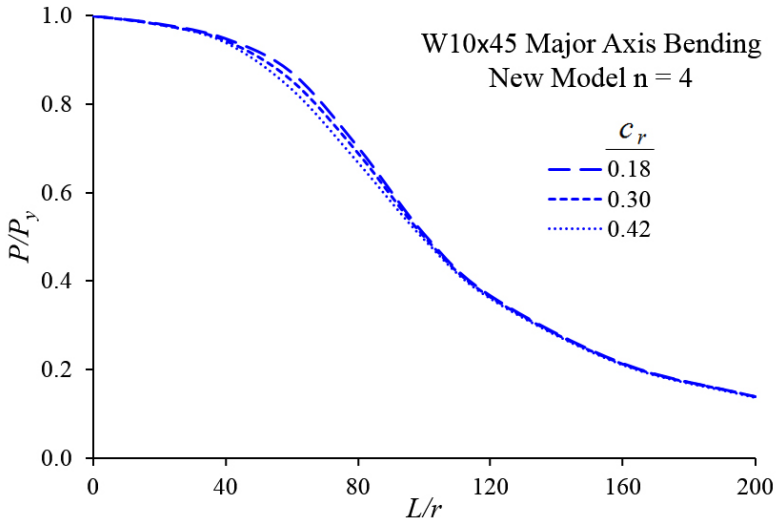

Figure 5: Column strength comparison of W8x31 with major-axis bending and three different c_r values

Figs. 6 and 7 are used to illustrate the stiffness reduction along the length of the column over a range of L/r values up to the limit load. As illustrated in Fig. 6, due to symmetry of the m conditions of a pinned-pinned column, the τ values are evaluated at five equally spaced locations from the mid-height to the bottom of the column over a range of L/r values from 40 to 200. Based on the p at the limit load and the m at each of the five locations on the column, the τ values were evaluated using the new material model for a W8x31 with minor-axis bending. In Fig. 6, the relative amount of flexural bending at the limit load is depicted for each L/r condition, and the gray shaded region in each column indicates the extent and location of relative stiffness reduction. It is noticed that significant stiffness reduction occurs over the full height of the column for $L/r = 40$ and 60, and for $L/r > 120$ where a purely elastic response is usually expected, there are small regions of inelastic response at the mid-section of the column.

Fig. 7 is used illustrate the stiffness reduction at the five locations along the height of the column as the axial load is increased to the limit load P for each L/r condition. All the points inside the triangular region bound by m_1 indicate an elastic ($\tau = 1$) response. It is noticed that the five points for all L/r conditions remain in this triangular region up to *2/3P*. Using Fig. 3a as a guide to understanding the stiffness reduction, the $L/r = 40$ and 60 conditions show all five points with significant stiffness reduction at high values of p and low values of m at the limit load. For the $L/r > 120$ conditions, several points near the mid-section of the column have inelastic response and thus slight stiffness reduction due to the relatively high values of m when the limit load is reached. As illustrated in Fig. 3a, these points correspond with τ values that are not as drastically reduced as those for $L/r < 60$ where at the limit load there is significant stiffness reduction over the full height of the column.

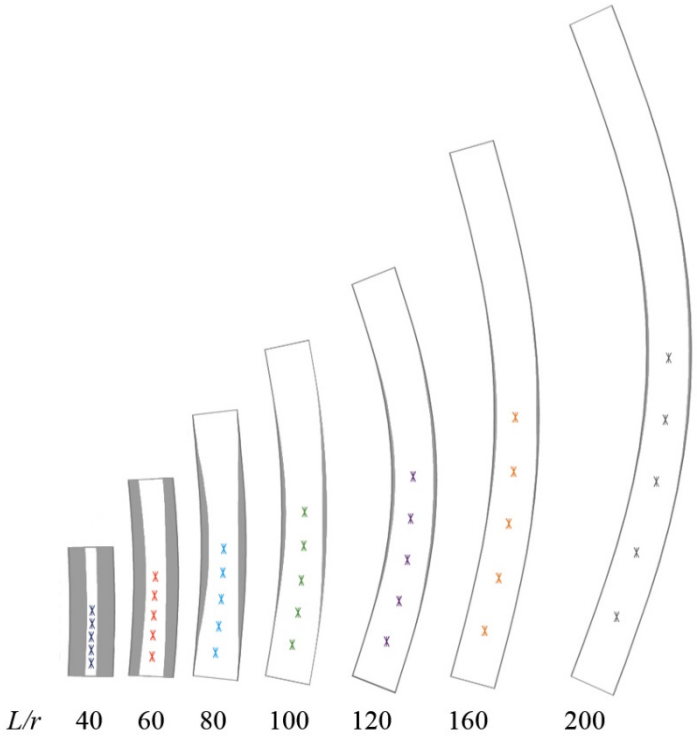

Figure 6: Extent and location of stiffness reduction of W8x31 over range of *L/r*

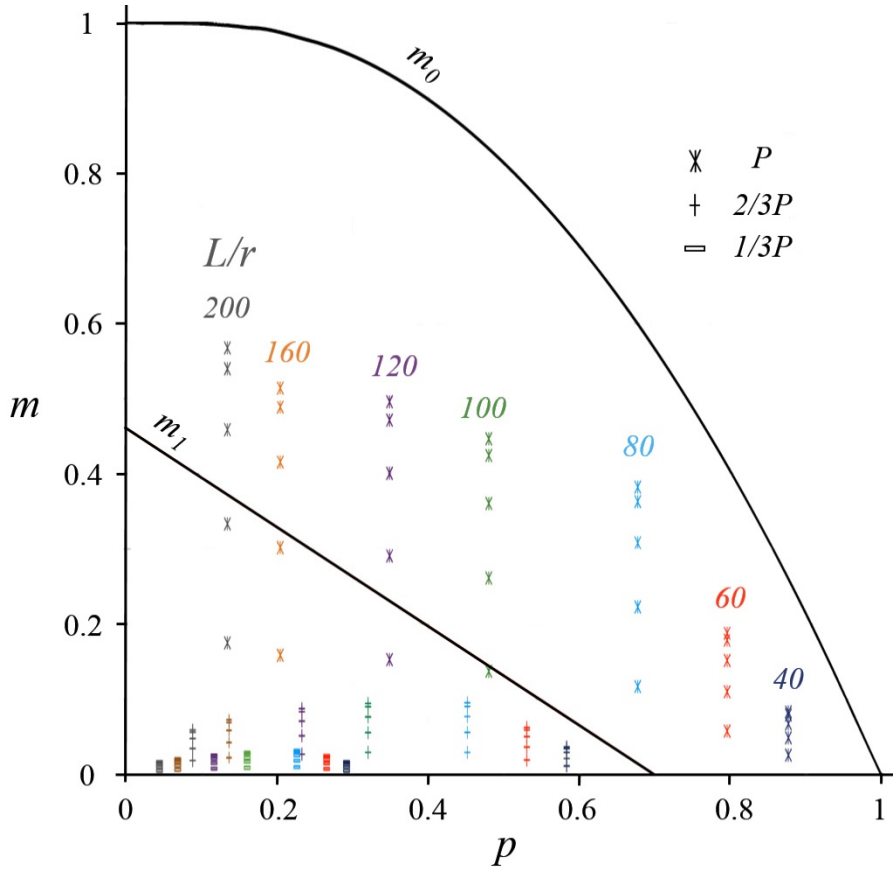

Figure 7: Stiffness reduction conditions of W8x31 with minor-axis bending over range of *L/r* values

Limit load analyses were conducted on a pinned-pinned W14x145 column using the new material model (Eqs. 10 and 11) and were compared with Eqs. (E3-2) and (E3-3) of the *Specification for Structural Steel Buildings* (2017) and the results obtained from an advanced nonlinear finite element model with an assumed residual stress pattern given by Galambos and Ketter (1959). The results for the major-axis bending condition are given in Fig. 8. The finite element model more closely follows the *Specification* curve, and that due to the error introduced by approximating the gray surface in Fig. 2 with the 3D surface in Fig. 3b, the new model with $n = 4$ gives slightly higher results up to approximately $L/r = 100$. All three curves are very similar for $L/r > 100$ where the response is primarily elastic along the length of the column.

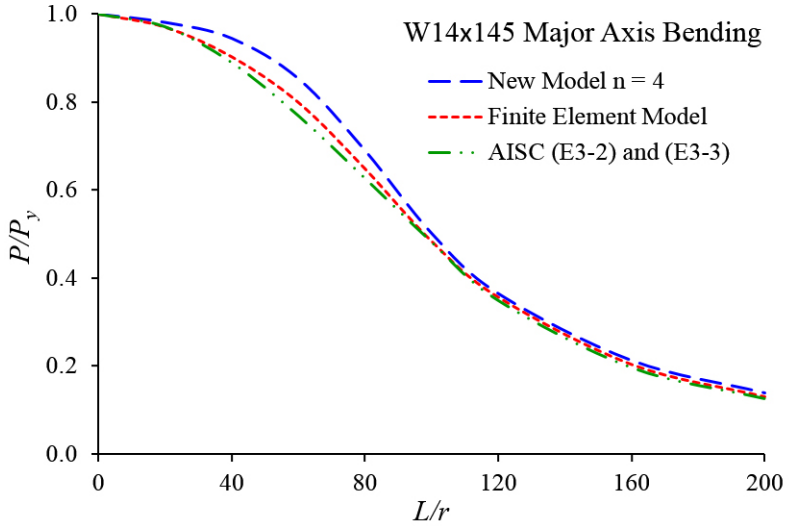

Figure 8: Column strength comparison of W14x145 with major-axis bending

The results for the minor-axis bending condition are given in Fig. 9. The finite element model gives results that are consistently below the *Specification* curve, and that due to the error introduced by approximating the gray surface in Fig. 1 with the 3D surface in Fig. 3a, the new model with $n = 2$ gives slightly lower results for $L/r < 50$ and slightly higher results for $50 < L/r < 100$.

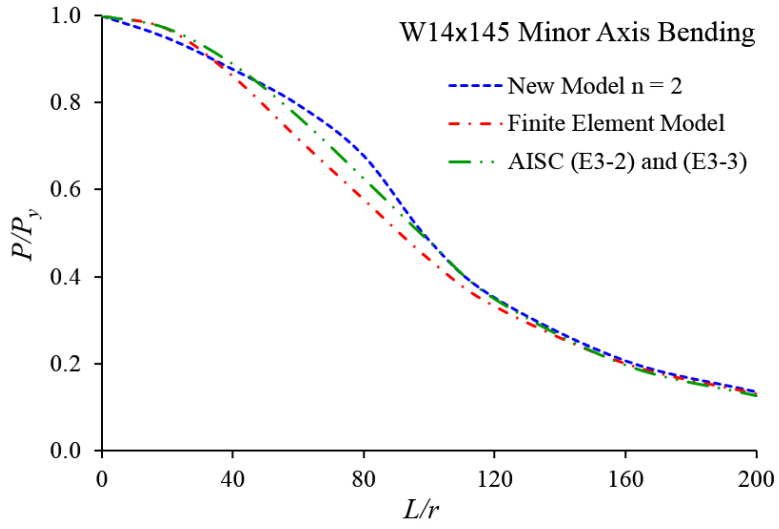

Figure 9: Column strength comparison of W14x145 with minor-axis bending

5. Test Frame Validation Study

System limit load analyses were conducted on five benchmark frames using the new material model (Eqs. 10 and 11) and were compared with the results obtained using advanced nonlinear finite element models. All of the member cross-sections were assumed to be fully-compact and their out-of-plane behavior fully restrained. All analyses were conducted using an advanced second-order inelastic analysis in accordance with Appendix 1 of the *Specification for Structural Steel Buildings* (2017). The modulus of elasticity and yield stress were reduced by a factor of 0.9, and the initial geometric imperfections were directly modeled using $L/500$ in the compounding direction. The test frames were modeled with *MASTAN2* using the new material model, and in all cases 10 line elements per member were used with $n = 2$ for minor-axis bending conditions and $n = 4$ for major-axis bending. The finite element models used an assumed residual stress pattern given by Galambos and Ketter (1959). All given factored loads were defined to result in a system limit load condition of the finite element models at an Applied Load Ratio (ALR) = 1.0.

The W-Shape member sizes, lengths and distributed loads of test frame 1a are given in Fig. 10. The beams and columns are oriented such that major-axis bending occurs in all members. Comparing the results in Fig. 11 between the nonlinear finite element model and the *MASTAN2* model, the lateral displacements at the top of frame 1a vary somewhat differently as the distributed loads are being fully applied, but the displacements are approximately the same when the system limit load is reached. The *MASTAN2* model reaches its limit load at ALR = 0.996.

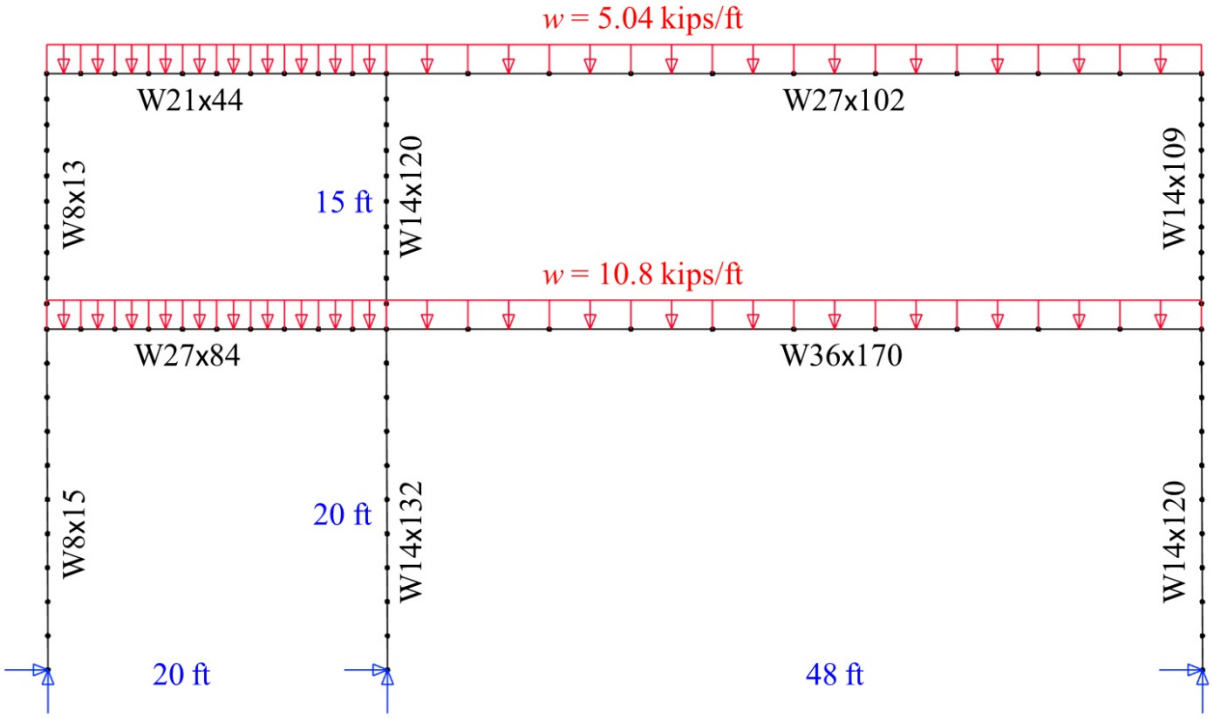

Figure 10: Test frame 1a

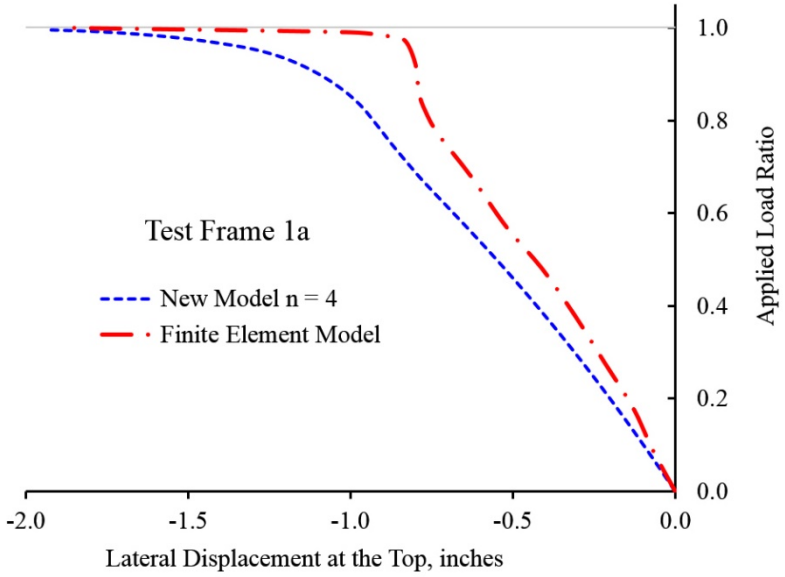

Figure 11: Applied load ratio vs. lateral displacement comparison for test frame 1a

The W-Shape member sizes, lengths and distributed loads of test frame 1b are given in Fig. 12. The beams are oriented such that major-axis bending occurs, and the columns are oriented such that minor-axis bending occurs. The results in Fig. 13 indicate that the lateral displacements at the top of frame 1b are similar between the two models and produce similar maximum displacements when the system limit load is reached. The *MASTAN2* model reaches its limit load at ALR = 1.04.

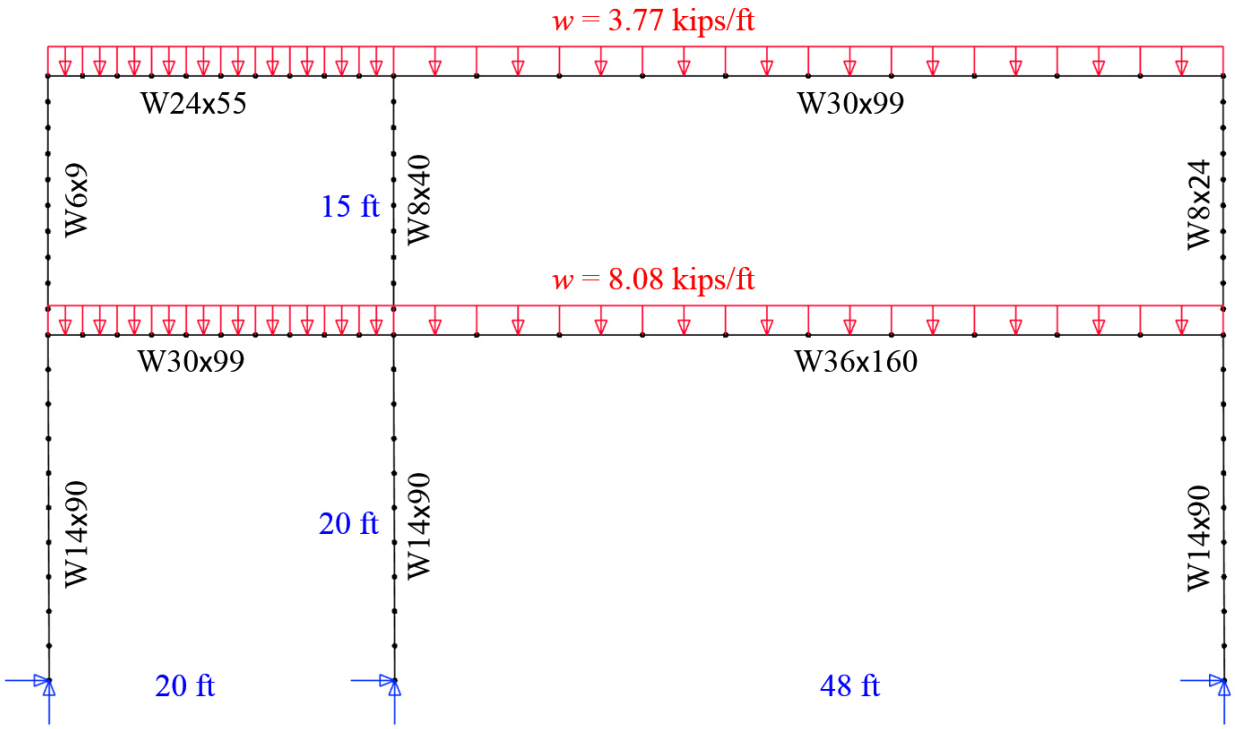

Figure 12: Test frame 1b

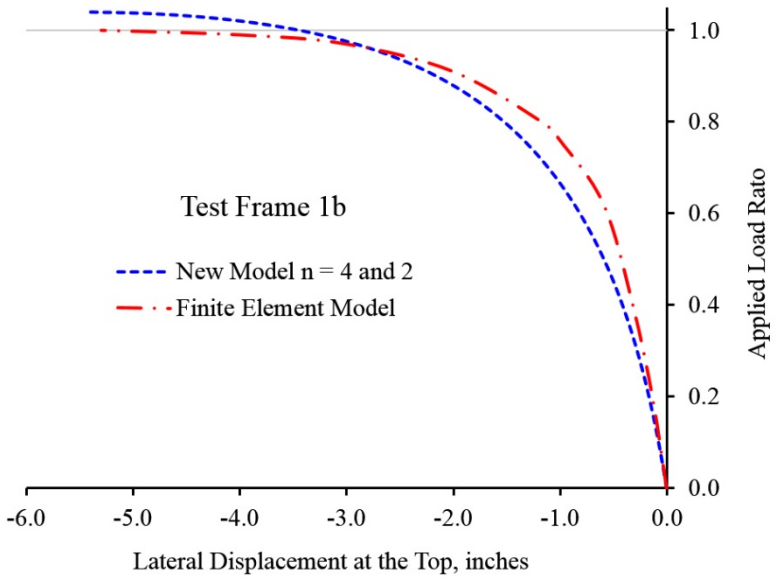

Figure 13: Applied load ratio vs. lateral displacement comparison for test frame 1b

The W-Shape member sizes, lengths and distributed loads of test frame 2 are given in Fig. 14. The beams and columns are oriented such that major-axis bending occurs in all members. The results in Fig. 15 indicate that the lateral displacements at the top of frame 2 are very similar between the two models as the loads are being applied and reach the similar maximum displacement values. The *MASTAN2* model reaches its limit load at ALR = 1.012.

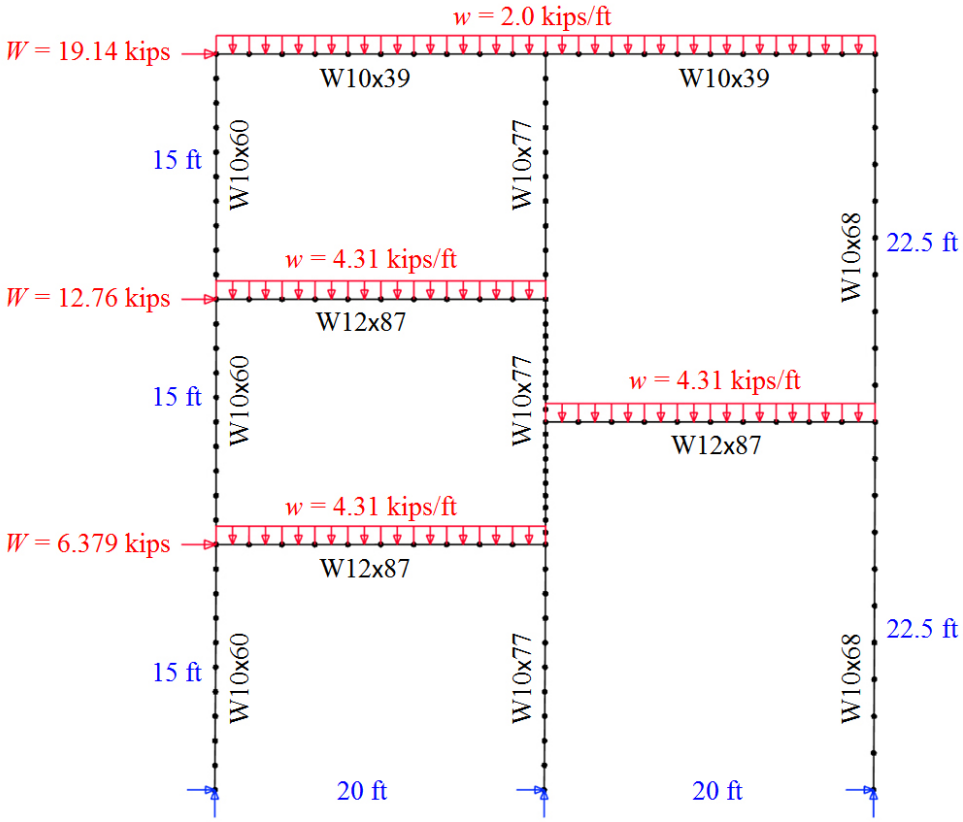

Figure 14: Test frame 2

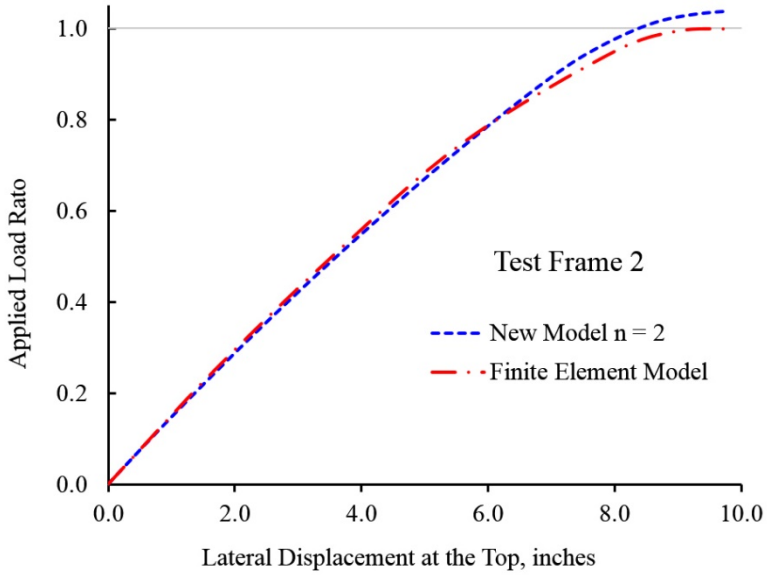

Figure 15: Applied load ratio vs. lateral displacement comparison for test frame 2

The W-Shape member sizes, lengths and distributed loads of test frame 3a are given in Fig. 16. The beams and columns are oriented such that major-axis bending occurs in all members. The results in Fig. 17 indicate that the lateral displacements at the top of frame 3a are very similar between the two models. The *MASTAN2* model reaches its limit load at ALR = 1.004.

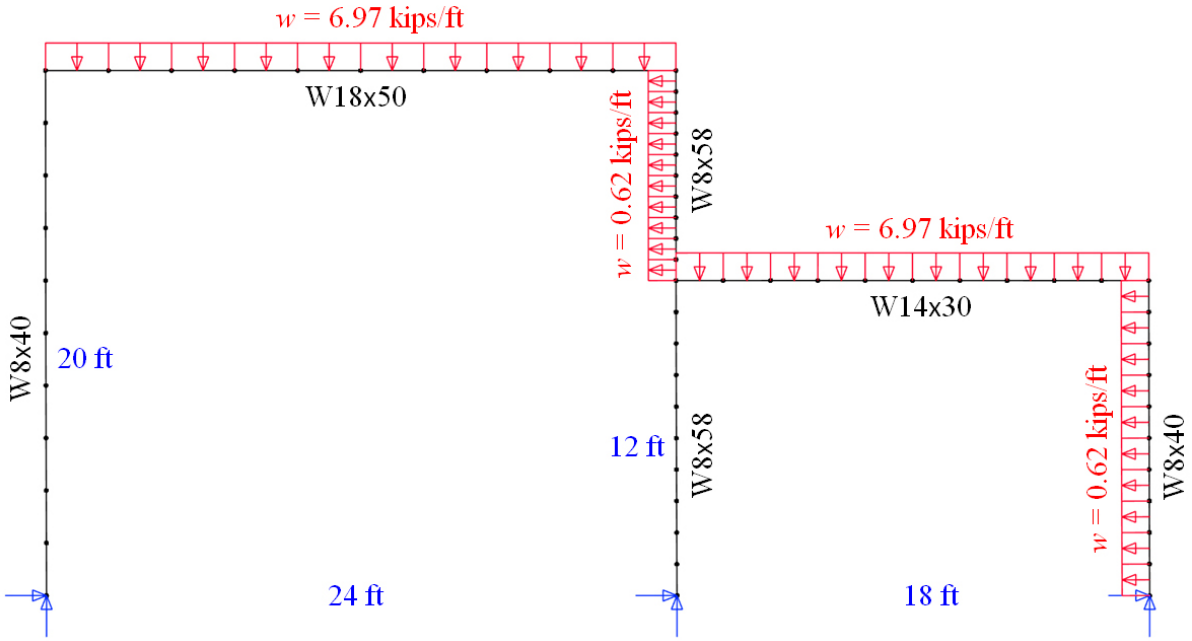

Figure 16: Test frame 3a

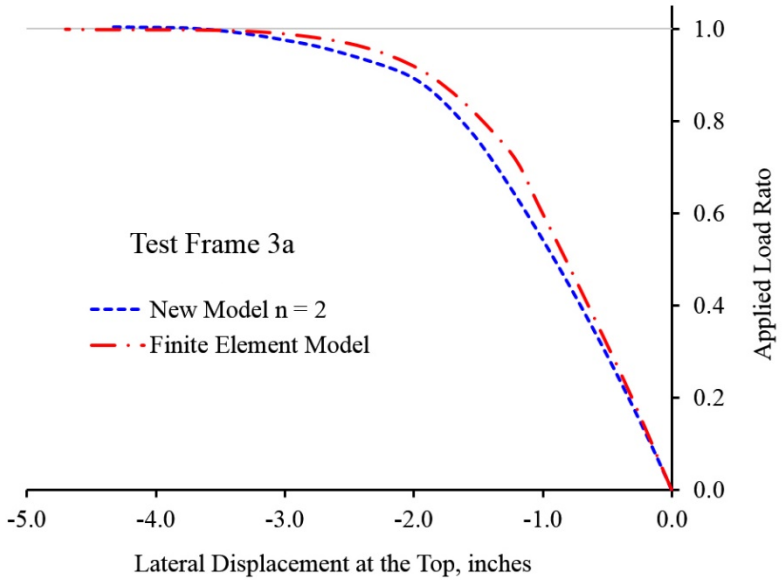

Figure 17: Applied load ratio vs. lateral displacement comparison for test frame 3a

The W-Shape member sizes, lengths and distributed loads of test frame 3b are given in Fig. 18. The beams and columns are oriented such that major-axis bending occurs in all members. The results in Fig. 19 indicate that the lateral displacements at the top of frame 3b between the two models are not as similar as the results obtained for frame 3a; however, they produce similar maximum displacement results when the system limit load is reached. The *MASTAN2* model reaches its limit load at ALR = 1.022.

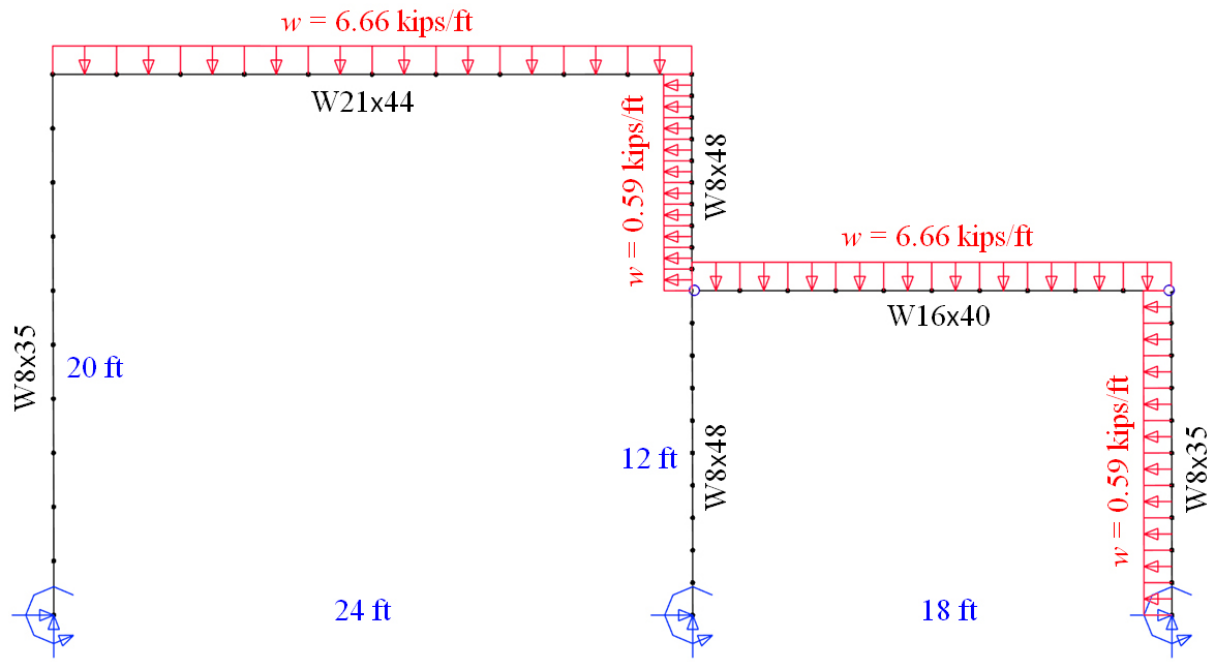

Figure 18: Applied load ratio vs. lateral displacement comparison for test frame 3b

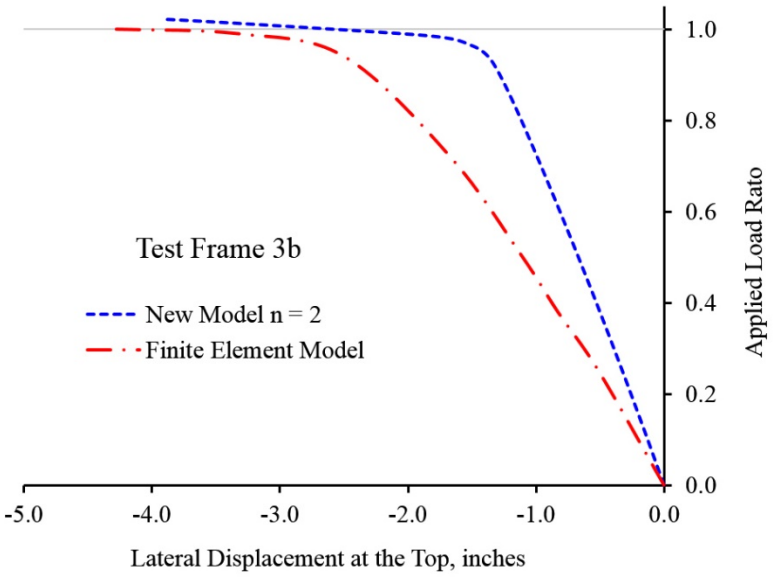

Figure 19: Applied load ratio vs. lateral displacement comparison for test frame 3b

6. Conclusions

This study investigated the effectiveness of a new inelastic material model to account for the loss of stiffness in W-Shape beam-columns with uniaxial bending and to use the model to determine the ultimate load capacity of steel frames. To approximate the stiffness reduction over the full range of m, p and c_r conditions, the new material model was developed from closed-form equations of the m-p-τ perimeter conditions. The stiffness reduction conditions between m_1 and τ_p to m_0 are based on approximate nonlinear equations that vary based on a given exponent n to account for the axis of bending and W-Shape cross-section dimensions. Since m_1 and τ_p are in the new material model, the τ results will always match the fiber element results up to the initial yield conditions, and since m_0 is also used, the τ results will always vary to the correct fully plastic m and p conditions for a given W-Shape and axis of bending.

The limit load column analyses indicate that the new material model provides results that are reasonable and consistent with known beam-column behavior. The limit load results at L/r values between 40 and 200 were used to gain insights into the extent and location of stiffness reduction that occurs over the height of the column. It was found that as the axial load approaches the limit load P, the response remains elastic up to $2/3P$ for all L/r conditions, and when performing a second-order inelastic analysis with initial geometric imperfections to determine the column limit load, there is no completely elastic response for L/r conditions up to 200. All five test frame results confirmed that the new material model provides close agreement with the limit load results obtained from using an advanced finite element model of the same frame conditions. Based on the results of the study, the new material model provides an effective means to account for the inelastic behavior of W-Shapes when using the provisions of Appendix 1 in the *Specification for Structural Steel Buildings*. Since the W-Shapes used in the study only considered $n = 2$ for minor-axis bending and $n = 4$ for major-axis bending, it is recommended that further research confirm that these values are adequate for the full range of W-Shapes used in construction.

References

Attalla M.R., Deierlein G.G., McGuire W. (1994). "Spread of plasticity: quasi-plastic-hinge approach." *Journal of Structural Engineering*, 120 (8) 2451-2473.

Chen W.F., Sohal I. (1995). *Plastic design and second-order analysis of streel frames*. Springer-Verlag, New York.

ECCS (1984). "Ultimate limit state calculation of sway frames with rigid joints." *TC 8 of European Convention for Constructional Steelwork (ECCS)*, No. 33.

Galambos T.V., Ketter R.L. (1959). "Columns under combined bending and thrust." *Journal of Engineering Mechanics*, 85: 1-30.

Kucukler M., Gardner L., Macaroni L. (2014). "A stiffness reduction method for the in-plane design of structural steel elements." *Engineering Structures*, 73: 72-84.

Kucukler M., Gardner L., Macaroni L. (2016). "Development and assessment of a practical stiffness reduction method for the in-plane design of steel frames." *Journal of Constructional Steel Research*, 126: 187-200.

Rosson B.T. (2016). "Elasto-plastic stress states and reduced flexural stiffness of steel beam-columns." *Proceedings of the 2016 SSRC Annual Stability Conference*, Orlando, Florida.

Rosson B.T. (2017). "Major and minor axis stiffness reduction of steel beam-columns under axial compression and tension conditions." *Proceedings of the 2017 SSRC Annual Stability Conference*, San Antonio, Texas.

Rosson B.T. (2018). "Modeling the influence of residual stress on the ultimate load conditions of steel frames." *Proceedings of the 2018 SSRC Annual Stability Conference*, Baltimore, Maryland.

Shayan S., Rasmussen, K.J.R., Zhang, H. (2014). "Probabilistic modeling of residual stress in advanced analysis of steel structures." *Journal of Constructional Steel Research*, 101: 407-414.

Steel Construction Manual, 15th Edition (2017). *Specification for Structural Steel Buildings*. AISC, Chicago.

Ziemian R.D., McGuire W. (2002). "Modified tangent modulus approach, a contribution to plastic hinge analysis." *Journal of Structural Engineering*, 128 (10) 1301-1307.

Ziemian R.D., McGuire W. (2015). *MASTAN2*, Version 3.5.

Zubydan A.H. (2011). "Inelastic second order analysis of steel frame elements flexed about minor axis." *Engineering Structures*, 33: 1240-1250.